


Electrocatalytic reaction-driven flow

Abimbola A. Ashaju , Jeffery A. Wood, and Rob G. H. Lammertink**Soft Matter, Fluidics and Interfaces, MESA+ Institute for Nanotechnology, University of Twente, Enschede, The Netherlands*

(Received 29 April 2020; accepted 1 April 2021; published 21 April 2021)

Immobilized electrocatalytic surfaces are capable of generating reaction-driven fluid flow by electrochemical energy conversion. A well-known system concerns the gold-platinum bimetallic motor driven by hydrogen peroxide conversion. In this work, we focus on experimental and numerical analyses that provide fundamental insight on the key elements that control the resulting transport characteristics in this system, including the generated electric field, reaction kinetics, and diffusio-electro-osmotic phenomena. The current between the electrodes and the induced potential that governs the reactive fluxes are measured electrochemically, while the fluid flow is analyzed using particle tracking velocimetry. Numerical simulations based on the Poisson-Nernst-Planck and Navier-Stokes equations reveal the interplay of the individual electrode surface reactivity, represented by the dimensionless Damköhler numbers, with the electrokinetic phenomena.

DOI: [10.1103/PhysRevFluids.6.044004](https://doi.org/10.1103/PhysRevFluids.6.044004)

I. INTRODUCTION

Nature has engineered nanoscale biological motors in form of microorganisms and proteins that are capable of converting chemical energy for complex molecular processes and biological functions [1,2]. Inspired by nature, researchers became actively involved in developmental activities where structures are synthesized, manipulated, and controlled at the molecular, atomic, and macromolecular scales for diverse applications. A good example is the locomotion of a catalytic nanorod within a fluid medium, which is powered by the conversion of chemical energy (fuel) that is harvested from the surrounding aqueous fluid [3–5]. The functionality of the nanorod has been adapted towards applications such as DNA detection, [6] cargo delivery [7–9], and rotary electromechanical devices [7].

The autonomous motion of catalytic nanorods has been observed and reported in the literature [3,10,11]. A single nanorod comprises a bimetallic duo that catalyzes the decomposition of a fuel, thereby creating the necessary gradients (concentration, potential) for its motion. During the electrochemical reaction at the two metals [e.g., platinum (Pt) and gold (Au)] with a hydrogen peroxide (H_2O_2) solution, oxidation occurs at the anode (platinum) yielding protons, electrons, and oxygen, while reduction takes place at the gold cathode where protons and electrons are consumed with water produced as a by-product (Fig. 1). The resulting ion and electron flow generates an electric field that is coupled with the local non-neutral fluid to create a body force that drives interfacial fluid motion.

Recent progress has expanded the application of nanomotors into microfluidics in the form of an immobilized system [12]. An immobilized nano-/micromotor can generate an interfacial convective fluid flow driven by electrochemical gradients that arise from electrocatalytic reactions. Immobilized micromotors (also known as micropumps) have been integrated into small confinements for

*Corresponding author: r.g.h.lammertink@utwente.nl

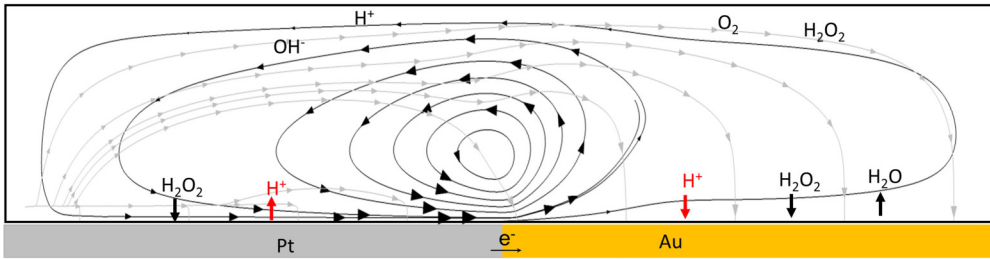


FIG. 1. A schematic that describes a Au-Pt reactive pair that catalytically decomposes H_2O_2 yielding reactive ionic species, which generates an electric field (gray streamlines) that drives fluid flow (black streamlines).

microscale fluid flow applications, which are capable of improving mass transport in areas impacted by boundary layer resistance [13]. Despite these advancements, some issues still limit the practical usage of an immobilized micromotor, especially its low energy conversion [12]. Understanding the fundamental parameters that drive the electrocatalytic reaction is necessary to fully exploit the fluid flow generated by an immobilized micromotor.

The literature that concerns catalytic micropumps comprises both experimental and numerical studies. In the experimental part we consider the electrochemical reaction that generates the electric field, which drives fluid flow. The metallic electrodes and electrolytes constitute altogether an electrochemical cell, whose characterization yields insight on the reaction mechanism that occurs at the electrode-electrolyte interface. The electrochemical reaction that actuates the catalytic micropump has been validated through the direct measurement of the catalytic current between the electrodes during the decomposition of H_2O_2 [4]. Tafel plots for anodic and cathodic reactions from Au and Pt electrodes were obtained from voltammetry measurements [10], from which the mixed potential that balances reactive fluxes was inferred. Furthermore, the Tafel plots identify the role of each metal via the anodic and cathodic branch, respectively, and the corresponding conversion rate via the current.

The proton flux that creates the electrical body force, which drives fluid flow, has been studied experimentally. Farniya *et al.* [14] imaged the concentration gradient that is generated during the electrochemical reaction using confocal fluorescence microscopy. They visualized the spatial variation of protons across the bioelectrode and quantified the amount that was generated and consumed under steady-state conditions. Moreover, they estimated the electrostatic potential distribution and electrode ζ potentials via the tracking of positively and negatively charged particles driven by a disk-shaped Pt-Au catalytic micropump. Simulations were fit to experimental measurements using the reaction rate constants, ion impurities, and surface ζ potential as fitting parameters. They imposed a fixed ζ potential value for the electrode in their simulations, and likewise that of the tracer particles for the fluid flow estimation and fluid pumping velocities up to $6 \mu\text{m/s}$ were deduced. A slight variation in electrolyte pH can have enormous consequences for the electrostatic potential and the fluid velocity as we will show.

Moran and Posner [15,16] developed a scaling analysis and performed numerical simulations that describe the movement of bimetallic nanorods fueled by H_2O_2 decomposition. They described how the nanorods motion is driven by the coupling of charge density and electric fields by solving the coupled Poisson-Nernst-Planck with Stokes equations and considered two specific forms of boundary conditions. First, they directly applied fixed fluxes on the electrodes and considered the rod to be uncharged by imposing a zero surface potential. Under this condition, the velocity field, albeit very small, near the rod showed a quadrupolar shape similar to induced charge electro-osmosis. Second, they relaxed the zero surface charge assumption and took into account the reaction kinetics, by introducing reactive flux expressions simplified from Butler-Volmer equations. This approach couples the reaction rate to the nanorods' surface potential as well as the evolution of reactants' concentrations on the nanorods' surface and led to realistic and more significant velocity

values. Both the sign and magnitude of the rod’s surface potential were found to play a determining role in its motion according to these simulations.

Esplandiu *et al.* [17] studied the fundamental parameters that govern the operation of a bimetallic micropump, and they attributed the fluid flow to be driven by self-induced electric field generated by the proton gradient across the electrodes. Their model ignored the water auto-ionization reaction. Davidson *et al.* [18] numerically analyzed reactivity patterns defined by the dimensionless Damköhler number that generates and depletes protons, which were related to the catalytic output of the bimetallic micropump. They also developed a simplified analytical model to predict the induced potential which balances electrode reactive fluxes and velocity flow magnitude.

This work performs a detailed experimental and numerical study of an immobilized electrocatalytic system under different surface reactivity regimes defined by the dimensionless Damköhler numbers. We characterize the electrochemical behavior of the electrocatalytic system through voltammetric Tafel analysis and direct potential measurement. Using particle tracking velocimetry we visualize the electrohydrodynamic response of the system and quantify the convective fluid flow. The induced fluid flow scales directly with the electrode ζ potential and the electric field according to Helmholtz-Smoluchowski equation. The zeta potential is highly sensitive to pH, which impacts the overall electrokinetic output. For this reason we measure the bielectrode ζ potential under pH conditions ranging from 2 to 10. Based on our experimental observations, a 2D numerical model that couples Poisson-Nernst-Planck and Navier-Stokes equations is solved for the potential, concentration, and velocity field under several reactive regimes while using experimental electrochemical data as a parameter input without any fitting parameter. Our numerical model advances existing numerical work by the inclusion of an electrode ζ potential that was measured experimentally under varying pH conditions.

II. EXPERIMENTAL SETUP

A. Chip fabrication

The Au and Pt electrode patterns were fabricated on borosilicate glass wafers via photolithography, metal sputtering, and lift-off. For each lift-off, positive resist was spun on the glass wafer, followed by ultraviolet exposure and development as described in [19]. Platinum and gold electrodes on tantalum (5 nm), an adhesive layer, were deposited by dc sputtering (MESA+ nanolab clearroom in-house equipment, “TCOathy”). Lift-off was performed with sonication in acetone. To investigate the diffusio-electro-osmotic phenomena, two design variants were fabricated: interdigitated electrodes (IDE) and Pt-Au bimetallic electrodes (Fig. 2). The IDE consists of electrode fingers of alternating Pt and Au connected to separate terminals. These electrode fingers have an interspacing of 40 μm and an electrode width of 50 μm . Each terminal is wire bonded to a printed circuit board. The bimetallic electrode consists of both Pt and Au in direct contact that forms a galvanic pair with a total length of 10 mm [Fig. 2(b)]. Prior to any experimental procedure, the electrodes were cleaned by rinsing with isopropyl alcohol and deionized water. The electrodes were then subjected to oxygen plasma (plasma power = 100 W, oxygen gas pressure = 0.5 bar, 5 min) to remove organic contaminants and photoresist residues [14].

B. Electrochemical characterization

The electrochemical experiments were conducted in a hydrogen peroxide solution (Sigma-Aldrich) using an Autolab PGSTAT204 potentiostat, running NOVA 2.0 software. Two forms of experiments were performed: induced potential measurement (IPM) and Tafel analysis. IPM was performed by measuring the potential difference between the short-circuited electrodes and the electrolyte during the electrochemical reaction [20]. This is shown schematically in Fig. 3, where the Pt/Au electrodes are connected to a single working electrode terminal of the potentiostat and the induced potential was measured against a micro-Ag/AgCl reference electrode (eDAQ model ET073).

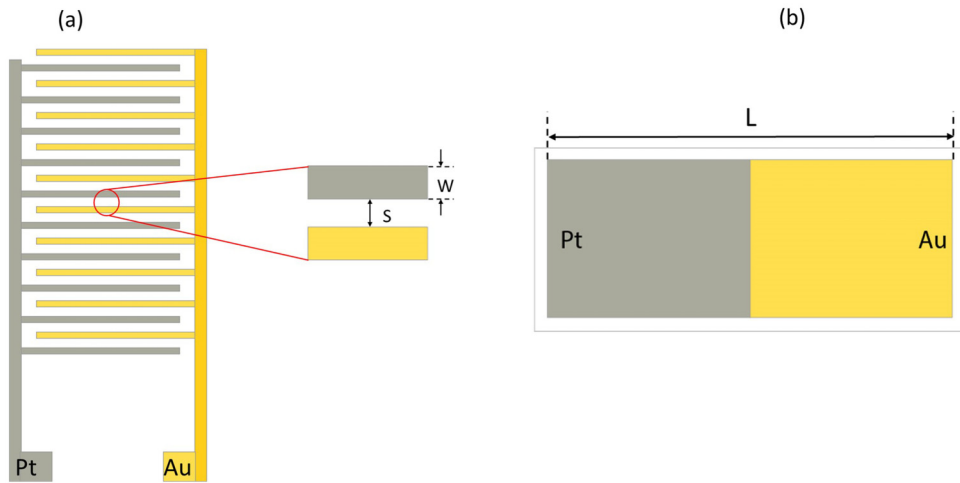


FIG. 2. Schematics showing the fabricated (a) interdigitated electrodes used for electrochemical measurement, with interspacing $S = 40 \mu\text{m}$ and electrode width $W = 50 \mu\text{m}$ and (b) Pt-Au bimetallic electrode for flow characterization experiments, having a total length $L = 10 \text{ mm}$.

Voltammetric experiments were performed for the Tafel analysis using a three-electrode system, where either of the two electrodes acts as the working electrode while the other is set as the auxiliary electrode (Fig. 3). The electrodes were polarized independently with potential sweeps within the oxidation and reduction range at a scan rate of 1 mV/s and their amperometric response is recorded [10].

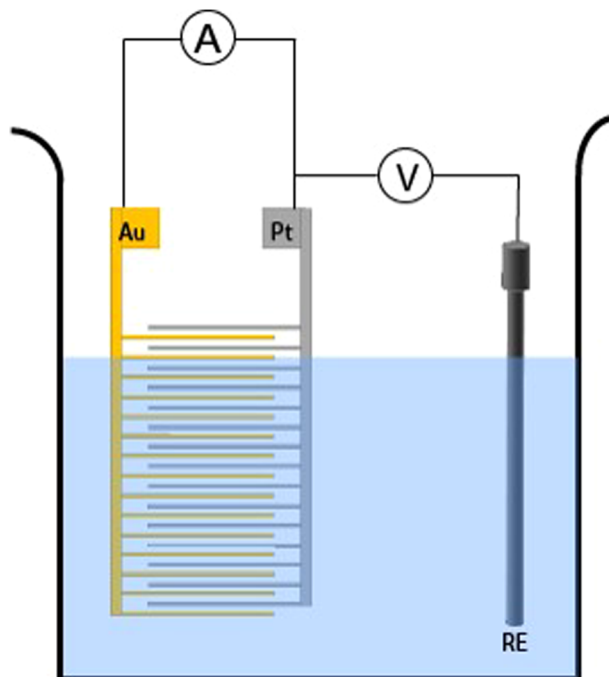


FIG. 3. Schematic representation of the electrochemical setup with the interdigitated electrodes.

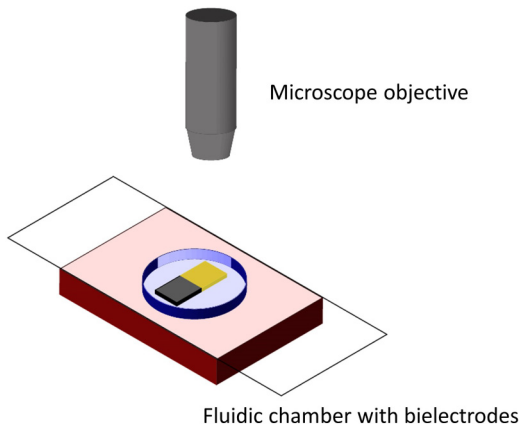


FIG. 4. A schematic diagram of the fluid flow experiment. The bimetallic electrode is sealed within a fluidic chamber with a cover glass slide.

C. Optical microscopy

Hydrogen peroxide solution (Sigma-Aldrich) was diluted to the desired concentration using MilliQ water (resistivity $\rho > 18 \text{ M}\Omega \text{ cm}$). We measured the conductivity of the peroxide solution that was prepared with deionized water, to be in the range of 10 to 30 $\mu\text{S/cm}$. Tracer particles [carboxylated-modified (FluoSpheres) and amidine latex beads (Fisher Scientific)], 1 μm in diameter, were seeded into the electrolyte and introduced into an imaging chamber (height $H = 1500 \mu\text{m}$) containing the bielectrode. The tracer particles were observed at 20 \times magnification using an inverted optical microscope (Carl Zeiss Axio Observer Z1) (Fig. 4), with images obtained at 10 fps. The particles trajectories were resolved using the general defocusing particle-tracking (GDPT) technique [21].

D. Tracer particles ζ potential measurement

The zeta potential of tracer particles used for fluid flow visualization was measured using a Zetasizer Nano ZS (Malvern Panalytical). Particle dispersions were prepared in MilliQ water and sonicated for 5 min. An ac electric field is applied to the colloidal dispersion, and the particle electrophoretic velocity is determined through laser Doppler velocimetry (LDV). During LDV, the moving particles are excited by a laser beam and diffuse light at frequencies that differ from the incident light. The frequency shift is proportional to the particles' velocity from which the electrophoretic mobility is determined ($\mathbf{u}_p = \mu_e E$). The ζ potential was calculated from the electrophoretic mobility with Henry's approximation $\mu_e = \frac{2\varepsilon\zeta f(ka)}{3\eta}$ based on Smoluchowski approximation, where μ_e is the electrophoretic mobility, $f(ka)$ is the Henry's function, ε is the permittivity, ζ is the zeta potential, and η is the viscosity of the fluid medium [22,23].

III. THEORY AND NUMERICAL SIMULATIONS

Numerical simulations were performed using COMSOL Multiphysics, a finite-element-based solver. We simulated a two-dimensional model with an aspect ratio of $H/L = 0.15$, which is representative of our experimental setup involving the bielectrode ($H = 1500 \mu\text{m}$, $L = 10\,000 \mu\text{m}$). The catalytic decomposition of H_2O_2 on a Pt-Au catalytic system is considered through oxidation and reduction pathways, given as



where oxidation occurs on platinum (the anode) and reduction takes place on Au (the cathode) [24].

We emphasize at this point that we focus on the simplest form of the electrochemical reaction that yields the generation and consumption of protons [15]. In our simulations we consider H^+ , OH^- , as well as Cl^- that results from the dissociation of HCl acid during the adjustment of the electrolyte's bulk pH.

A. Poisson-Nernst Planck and Stokes equations

The electrokinetic phenomena exhibited by the Pt/Au system is solved and described by the coupled Poisson-Nernst-Planck and Stokes equations. This approach has been used in other works to simulate the locomotion of nanorods [16] and catalytically induced flows [17,18]. The dimensionless forms of the governing equations are presented in Eqs. (3)–(6), and more details on its derivation and transformation can be found in Druzgalski *et al.* [25].

The dimensionless Poisson equation [Eq. (3)] solves for the induced potential, whose gradient yields the electric field together with the local charge density. The Poisson equation is coupled with the ionic species transport to resolve the electrical double layer formed during the electrochemical reaction at the electrode-electrolyte interface. The dimensionless Debye length $\epsilon = \frac{L_D}{L}$ whose value is selected to ensure numerical stability, where L is the bielectrode total length, $L_D = \sqrt{\frac{\epsilon V_T}{2F\tilde{c}_\infty}}$ is the Debye length, usually hundreds of nanometers for low salt concentration, and \tilde{c}_∞ is the bulk proton concentration:

$$-2\epsilon^2 \nabla^2 \phi = \sum_i z_i c_i, \quad (3)$$

where $\phi = \frac{\tilde{\phi}}{V_T}$ is the dimensionless electrostatic potential obtained by normalizing the electrostatic potential by the thermal voltage $V_T = \frac{RT}{F} \approx 25$ mV, T is the temperature, F is the Faraday constant, and R is the universal gas constant. The tilde symbol ($\tilde{}$) implies a dimensional quantity.

The dimensionless Nernst-Planck equation describes the ionic species transport by solving the advection-diffusion and electromigration contributions [Eq. (4)], where \mathbf{u} is the fluid velocity and $c_i = \frac{\tilde{c}_i}{\tilde{c}_w}$ is the concentration of species i normalized by the bulk concentrations of H^+ and OH^- in pure water ($\tilde{c}_w = 1 \times 10^{-7}$ M), having a diffusion constant $D_i = \frac{\tilde{D}_i}{D_0}$ with valence z_i . \tilde{D}_0 is the diffusivity of hydroxide ($\tilde{D}_0 = 5.273 \times 10^{-9}$ m²/s) ions chosen as an arbitrary reference value. $R_i = \text{Da}_b (\frac{K_w}{\tilde{c}_\infty} - c_{\text{H}^+} c_{\text{OH}^-})$ is a bulk reaction term that enforces water autoionization for H^+ and OH^- . K_w is the water ionization constant expressed as $K_w = [\text{H}^+][\text{OH}^-] = 1 \times 10^{-14}$ M². Da_b is the bulk Damköhler number defined as $\text{Da}_b = \frac{k_b L^2 \tilde{c}_\infty}{D_0}$, where k_b is the water recombination reaction rate constant, and c_{H^+} and c_{OH^-} are proton and hydroxide species concentrations:

$$\frac{\partial c_i}{\partial t} + \nabla \cdot (\mathbf{u} c_i) = D_i \nabla \cdot (\nabla c_i + z_i c_i \nabla \phi) + R_i. \quad (4)$$

The fluid flow is assumed laminar and incompressible, giving rise to the Stokes and continuity equations [Eqs. (5) and (6)], where Sc is the Schmidt number defined as $\text{Sc} = \frac{\mu}{\rho D_0}$ and of $O(10^3)$.

The electro-hydrodynamic coupling constant is defined as $\kappa = \frac{\epsilon V_T^2}{\mu D_0}$ and is typically fixed by the aqueous electrolyte properties:

$$\frac{1}{\text{Sc}} \frac{\partial \mathbf{u}}{\partial t} = -\nabla p + \nabla^2 \mathbf{u} - \frac{\kappa}{2\epsilon^2} \rho_e \nabla \phi, \quad (5)$$

$$\nabla \cdot \mathbf{u} = 0. \quad (6)$$

B. Acid-base equilibria and initial concentrations

In our experimental study, we adjusted the starting pH of the H_2O_2 solution by the addition of HCl, yielding H^+ and Cl^- . Cl^- is included as inert species in the model whose initial concentration is fixed by the value of the bulk electrolyte pH. We derive an expression that relates the initial

proton concentration, \tilde{c}_{H^+} depending on the bulk pH and other limiting conditions involving water equilibrium and electroneutrality (7) (see Appendix A):

$$\tilde{c}_{\text{H}^+} = \frac{\tilde{c}_{\infty} + \sqrt{(\tilde{c}_{\infty})^2 + (4K_w)}}{2} \quad (7)$$

C. Surface reactivity pattern

The surface reactivity is represented by the dimensionless Damköhler number Da that relates the electrocatalytic reaction timescales to diffusive transport timescales [15]. It can be defined for individual electrodes in the catalytic system as the anodic Da_a and cathodic Da_c Damköhler number shown in Eqs. (8) and (9). Variation of these respective Da numbers will create reaction regimes that highlight the role of each electrode on proton generation and depletion:

$$Da_a = \frac{k_a L \tilde{c}_{\text{H}_2\text{O}_2}}{\tilde{D}_+ \tilde{c}_{\infty}}, \quad (8)$$

$$Da_c = \frac{k_c L \tilde{c}_{\infty} \tilde{c}_{\text{H}_2\text{O}_2}}{\tilde{D}_+}. \quad (9)$$

The anodic and cathodic rate constants are denoted by k_a and k_c , respectively, $\tilde{c}_{\text{H}_2\text{O}_2}$ is the concentration of H_2O_2 , \tilde{D}_+ is the proton diffusivity constant ($\tilde{D}_+ = 9.3 \times 10^{-9} \text{ m}^2/\text{s}$), and \tilde{c}_{∞} is the bulk proton concentration that is fixed by the pH of the solution.

D. Boundary conditions

We apply a no-slip condition, $\mathbf{u} = 0$, on all boundaries. The electrical double layer induced during the electrochemical reaction at the electrode-electrolyte interface is divided into two regions: the Stern and diffuse layer [26]. Our model explicitly resolves the diffuse layer part of the electric double layer, while the Stern layer contribution is resolved by scaling the potential drop across the Stern layer ($\Delta\phi_S$) with the zeta potential ζ [Eq. (11)] and the Debye length [15,17]:

$$\Delta\phi_S = \zeta - \phi_{\text{electrode}}, \quad (10)$$

$$\Delta\phi_S \approx \frac{\lambda_S}{\lambda_D} \zeta. \quad (11)$$

At low salt concentrations $\frac{\lambda_S}{\lambda_D} \ll 1$, and $\Delta\phi_S$ is extremely small, hence $\phi_{\text{electrode}} \cong \zeta$, where λ_S and λ_D are the Stern layer and Debye thickness. The potential boundary condition at the surface of the electrodes ($y = 0$) is defined by their respective ζ potential as $\phi_{\text{Pt}} = \zeta_{\text{Pt}}$, and $\phi_{\text{Au}} = \zeta_{\text{Au}}$. The zeta potential associated with each electrode has been experimentally deduced from the streaming current (see Appendix B) and was found to be highly dependent on pH (Fig. 11). For this reason, the potential boundary condition is coupled to the ζ potential of the appropriate electrode, which corresponds to a certain pH in the model using a mixed Neumann/Dirichlet boundary condition. The boundary condition at the upper boundary is defined as $\frac{\partial\phi}{\partial y} = 0$.

The initial concentration for individual ionic specie depends strongly on the bulk electrolyte pH $[-\log_{10}(\tilde{c}_{\infty})]$, and is applied as a Dirichlet condition at the uppermost boundary of the model. Anions are inactive during the electrocatalytic reaction, and hence their flux is set to zero [see Eqs. (12) and (13)]:

$$n \cdot j_{\text{OH}^-} = n \cdot (D_{\text{OH}^-} \nabla c_{\text{OH}^-} + z_{\text{OH}^-} c_{\text{OH}^-} \nabla\phi - \mathbf{u} c_{\text{OH}^-}) = 0, \quad (12)$$

$$n \cdot j_{\text{Cl}^-} = n \cdot (D_{\text{Cl}^-} \nabla c_{\text{Cl}^-} + z_{\text{Cl}^-} c_{\text{Cl}^-} \nabla\phi - \mathbf{u} c_{\text{Cl}^-}) = 0. \quad (13)$$

The electrochemical reaction flux that occurs at the electrode/electrolyte interface has been reformulated from the Frumkin-Butler-Volmer equation [15]. We apply the proton flux boundary

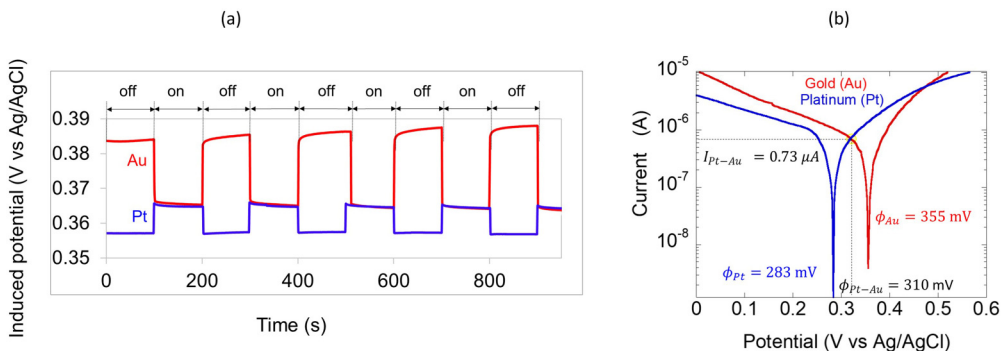


FIG. 5. Representative plots for (a) induced potential vs time for the interdigitated electrodes in 0.325 M H_2O_2 during the on and off mode and (b) Tafel plots for Au-Pt interdigitated electrodes in 0.325 M H_2O_2 .

condition on Pt and Au, which has been derived by matching the combined diffusive and electromigration fluxes with the electrocatalytic reaction flux [18], where j_{H^+} refers to proton flux across the electrodes (14), and j_{Pt} and j_{Au} are defined as platinum and gold surface proton flux respectively:

$$n \cdot j_{\text{H}^+} = n \cdot (D_{\text{H}^+} \nabla c_{\text{H}^+} + z_{\text{H}^+} c_{\text{H}^+} \nabla \phi - \mathbf{u} c_{\text{H}^+}) = \begin{cases} j_{\text{Pt}} = D_{\text{H}^+} \text{Da}_a \\ j_{\text{Au}} = D_{\text{H}^+} \text{Da}_c c_{\text{H}^+}^2. \end{cases} \quad (14)$$

E. Mesh independence

The commercial finite element method software COMSOL Multiphysics 5.0 was used in solving the dimensionless governing equations. To confirm mesh independence, the simulation was run on mesh element numbers ranging from 1.5×10^4 to 2.6×10^5 . Mesh independence is observed as from $N = 10^5$ elements, and further mesh refinement yielded velocities that varied less than 1%. To strike a compromise between solution accuracy and computation time, the element number was chosen at $N = 10^5$, with the mesh refined around the electrodes region to accurately capture the electric double layer and to resolve the electrical and concentration gradients occurring at the electrode-electrolyte interface.

IV. RESULTS AND DISCUSSION

A. Electrochemical mechanism

When the interdigitated electrodes are connected and immersed in H_2O_2 solution, anodic and cathodic reactions occur [27]. A common potential is generated for the electrodes during the electrochemical reaction that balances reactive fluxes on both electrodes. By connecting and disconnecting interdigitated electrodes repeatedly at certain time intervals, the induced potential is always regenerated during the connected mode, while the open circuit potential for individual electrodes is observed during the off mode [Fig. 5(a)]. Moreover, the induced potential shows sensitivity to the mode of operation and confirms the electrochemical decomposition of H_2O_2 as the basis for electrocatalytic actuation.

Figure 5(b) shows the Tafel plots for Pt and Au electrodes in 0.325 M H_2O_2 , representing the electrochemical current versus the applied potential. In these measurements, the potential of each electrode is varied and the current response is obtained. The Tafel curve for each individual electrode consists of anodic and cathodic branches that correspond to oxidation and reduction pathways, respectively. The sharp dip in each current response indicates the mixed potential where the net current is zero. At this potential, the transition from oxidation to reduction and vice versa occurs [28]. The mixed potential describes the role of each electrode if they are electrically connected and thus at the same potential [10]. Gold acts as the cathode, and platinum as the anode. The point

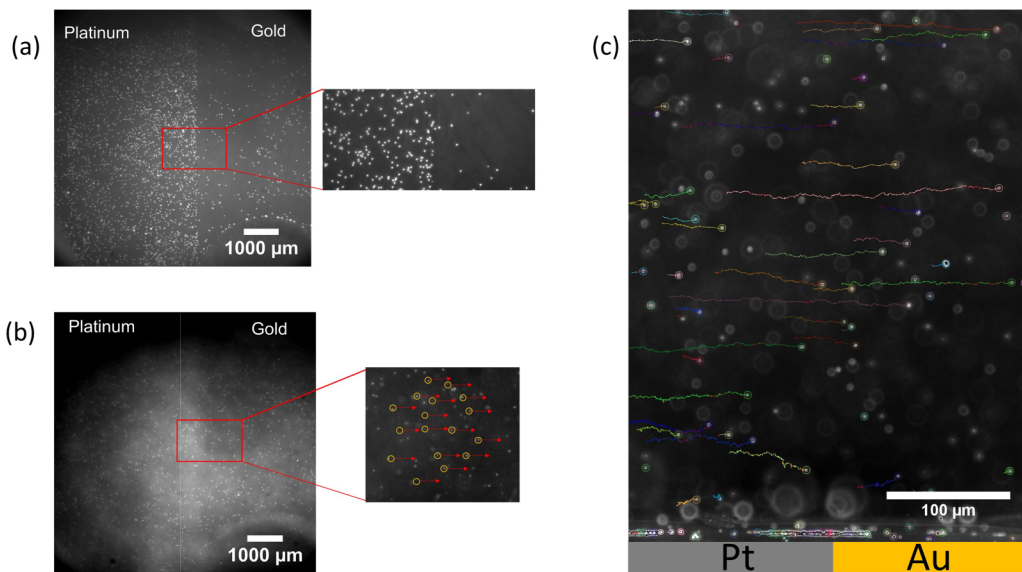


FIG. 6. Fluid flow visualization by particle tracking. (a) Formation of colloidal patterns on the bimetallic electrode due to an electrostatic force. (b) Colloidal particles driven by catalytically induced fluid flow near the electrode's surface region. (c) Particle tracks for fluid flow observed from the electrode side view.

at which both voltammetric profiles intersect yields the catalytic current ($0.73 \mu\text{A}$) and bimetallic potential (310 mV) arising from a connected Pt-Au electrode system.

The bimetallic potential that was obtained from the Tafel plots is comparable to the induced potential measurement. Accordingly, both techniques are appropriate for quantifying the induced potential that enforces current conservation across the bielectrode.

B. Fluid flow visualization and quantification

When a suspension of tracer particles and H_2O_2 was fed into the chamber, a combined mechanism of electrostatic and hydrodynamic interactions occurs near the electrode region (Fig. 6). The negatively charged particles migrate to both the Pt and Au electrodes and eventually become trapped owing to a strong electrophoretic force close to the surface of the bielectrode. They form patterns and aggregates that highlight the junction between Pt and Au electrodes [Fig. 6(a)]. Near the surface, the particles are transported from Pt to Au, while the opposite movement occurs at the upper region of the channel [Fig. 6(b); Supplemental Material video 1 [29]].

The pattern of fluid movement is verified by imaging from the side view near the connected electrodes region. The particle transport tracks that are obtained by superimposing image frames (imageJ particle tracker) [30] confirm fluid flow from Pt to Au [Fig. 6(c)].

The observed particle velocities \mathbf{u}_p consist of both the electrophoretic \mathbf{u}_{ep} and the fluid flow \mathbf{u}_f components [Eq. (15)]. Decoupling these yields the actual magnitude of the catalytically induced fluid flow. This can be realized by using the two-particle correlation [14,31], where two particles similar in size and having different electrophoretic mobilities can be used in determining the fluid flow under the same experimental conditions. The particle velocity for the different tracer particles (here positive and negative) are defined in Eqs. (16) and (17) to yield the fluid flow velocity [Eq. (18)]:

$$\mathbf{u}_p = \mathbf{u}_{ep} + \mathbf{u}_f, \quad (15)$$

$$\mathbf{u}_{p+} = -\frac{\varepsilon}{\eta} \zeta_{p+} E + \mathbf{u}_f, \quad (16)$$

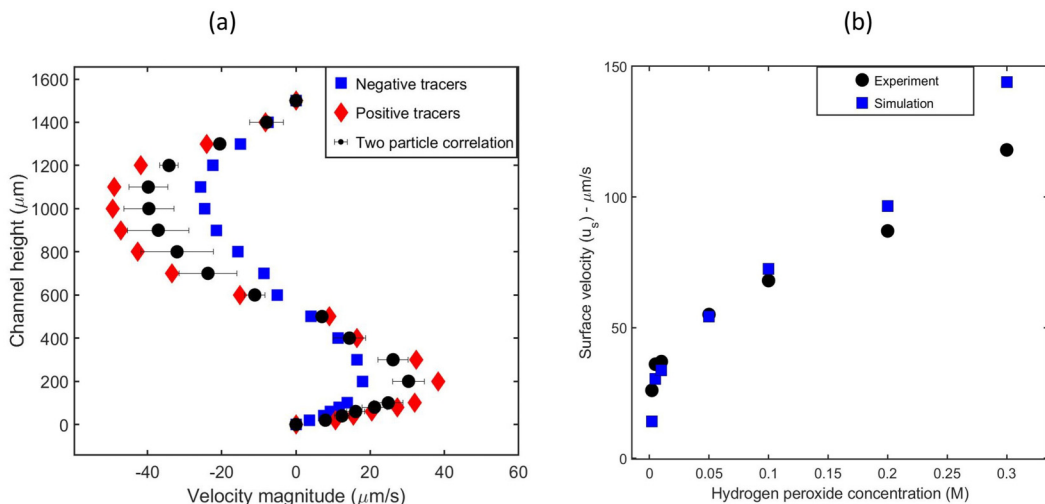


FIG. 7. (a) Two-particle correlation velocimetry used in determining the flow velocity, for 0.3 M H₂O₂, pH 6. The particle velocities are plotted as a function of the channel height. Flow near the surface of the bielectrode is driven from Pt to Au, while the opposite movement is obtained at the upper part of the channel due to fluid continuity. Error bars represents standard deviations from triplicate measurements. (b) Comparison of experimentally estimated surface fluid velocity u_s with simulation result as a function of H₂O₂ concentration.

$$\mathbf{u}_{p-} = \frac{\varepsilon}{\eta} \zeta_{p-} E + \mathbf{u}_f, \quad (17)$$

$$\mathbf{u}_f = \frac{\zeta_{p+} \mathbf{u}_{p-} - \zeta_{p-} \mathbf{u}_{p+}}{\zeta_{p+} - \zeta_{p-}}, \quad (18)$$

where ζ_{p+} and ζ_{p-} correspond to the ζ potentials for the positive and negative particles respectively (see Fig. 12, Appendix C), η is the fluid viscosity, and ε is the permittivity of the fluid (7.10×10^{-10} F/m).

Figure 7(a) shows the particle velocity profiles along the channel height from the bielectrode junction. The velocity of the positive tracers exceeds that of the negative tracers due to the interaction between the induced electric field and the ζ potential of the particles, which creates an electrophoretic force that enhances the movement of the positive particles. In the case of the negative tracers, the electrophoretic force retards the movement of the particles with respect to the fluid flow. The positive and negative tracers velocities were averaged at every height and solved with the two-particle correlation (18) to extract the fluid flow that presents a similar profile. The fluid flow at the bielectrode region is driven from the anode to the cathode in the positive sense, while the negative flow recorded at higher heights occurs in the opposite direction due to flow continuity within the confined channel.

We compare our estimated experimental fluid velocity (inferred from the particle tracer velocities) with our numerical simulation for the case of 0.3 M H₂O₂, pH 6. Figure 14 shows a strong quantitative similarity between both flow profiles, except for the near electrode region. The deviation results from a strong electrophoretic force that impacts particle motion around the electrode surface region.

We determined the electrophoretic force for both negative and positive tracers and compared these with the fluid drag force at each location in Fig. 13 (see Appendix D). At the lower part of the channel ($y \leq 400 \mu\text{m}$), the electrophoretic force becomes dominant. Near the surface of the bielectrode ($y \leq 25 \mu\text{m}$) the electrophoretic force becomes amplified by the strong electric field and affects the movement of the charged particles in conjunction with the fluid drag force. Very

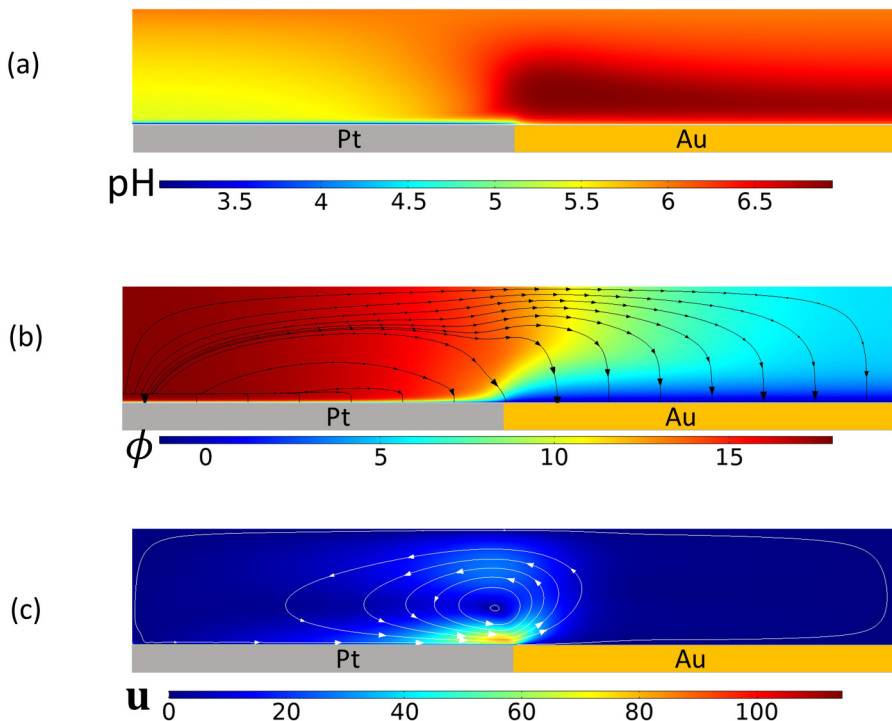


FIG. 8. Simulation field results for $Da_a = 350$, $Da_c = 1$, 2 mM H_2O_2 , pH 6: (a) proton spatial distribution indicated by pH value; (b) dimensionless induced potential overlaid by electric field streamlines, generated by proton flux (arrows); (c) dimensionless velocity magnitude with streamlines.

near the electrodes, the electrophoretic force can be an order of magnitude higher than the drag force, which results in fluid flow retardation and high offset between simulations and experimentally inferred velocities. To circumvent this problem, a simple analytical expression was fitted with the upper parabolic part of the experimental fluid flow velocity ($y \geq 600 \mu\text{m}$) where the influence of the electrophoretic force is less severe (see Appendix D). The fit obtains a surface velocity u_s that is comparable with the maximum velocity obtained from the simulation (Fig. 14). We investigated the dependence of the surface velocity on the concentration of H_2O_2 that fuels the reaction. Both experimental and simulation results indicate that the induced velocity increases with H_2O_2 concentration [Fig. 7(b)].

C. Numerical simulations

In order to understand further our experimental observations, simulations were conducted using our electrochemically measured current $0.6 \mu\text{A}$ (for 2 mM H_2O_2 and pH = 6) as an input parameter. The current was converted to molar flux ($\text{mol}/\text{m}^2 \text{ s}$) and applied directly as an electrode boundary condition in the model. The effective rate constants for the oxidation and reduction reactions are extracted from the simulation results by applying the Frumkin-corrected Butler-Volmer equation [Eq. (19)] which has been adopted in other works for investigating transport phenomena near electrodes [15,32–34]:

$$j = k_a \tilde{c}_R \exp \left[\frac{(1 - \alpha)mF \Delta \tilde{\phi}}{RT} \right] - k_c \tilde{c}_O \exp \left(\frac{-\alpha mF \Delta \tilde{\phi}}{RT} \right). \quad (19)$$

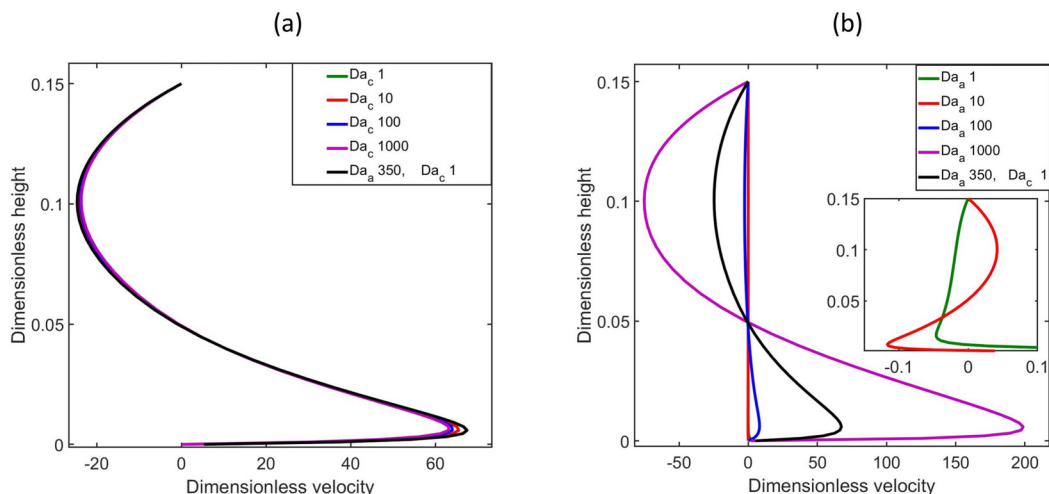


FIG. 9. Variation of the axial flow velocity along the y -axis from electrodes' junction for (a) cathodic Damköhler numbers Da_c and (b) anodic Damköhler number Da_a . Inset: flow reversal at $Da_a < 100$.

Here j_{H^+} is the proton flux expressed from the measured current density through Faraday's law, and m is the number of electrons transferred during the reaction. The generalized oxidation and reduction reactants' concentration are \tilde{c}_O and \tilde{c}_R , k_a is the anodic rate constant ($k_a = 1.63 \times 10^{-7}$ m/s), and k_c is the cathodic rate constant ($k_c = 5.16 \times 10^{-4}$ m⁷ s⁻¹ mol⁻²). These rate constants are used in determining the respective Damköhler numbers, which are defined in Eqs. (8) and (9). The Damköhler numbers are calculated to be $Da_a = 350$ and $Da_c = 1$, respectively. The ζ potential for Au and Pt electrodes that corresponds to the bulk electrolyte pH are directly inferred from Fig. 13 to be approximately (-32 mV and -33 mV), respectively.

Figure 8(a) shows the pH profile that highlights the proton gradient that is spatially established across the electrodes during the steady-state reaction. Proton generation at the anode (Pt) is indicated by a low pH while protons are depleted at the cathode (Au). Figure 8(b) shows the induced electric potential, overlaid with electric field lines that results from the proton gradient. The electric field originates from the anode and points towards the cathode. The product of the electric field with local charge density creates a body force that drives fluid flow, whose magnitude appears to be maximum around the junction of the connected electrodes [Fig. 8(c)]. The fluid flow streamlines confirm the direction of the fluid movement, from the anode to the cathode, and recirculated within a closed system to fulfill continuity. These electrokinetic observations are coupled, autonomous, and self-driven by the electrocatalytic reactions.

Further simulations were performed by keeping either of the experimentally determined Damköhler numbers constant while solving the other over a specified range. The variation of these numbers, which may be difficult to realize experimentally, gives more insight on our experimental observations. The resulting axial velocities $u(y)$ are plotted along the vertical direction from the electrodes (Fig. 9).

In the case where Da_c is varied [Fig. 9(a)], the induced velocity is inversely proportional to an increase in Da_c . At $Da_c > 1000$, the anodic oxidation reaction limits the overall catalytic process because it is incapable of dealing with the cathodic demands. Consequently, the proton gradient that generates the electrical body force becomes weak, and the induced velocity decreases in magnitude.

The variation of Da_a presents interesting observations on the induced velocity [Fig. 9(b)]. In the case of $Da_a \geq 100$, the velocity flow profiles are similar to the Da_c controlled reactions where the flow is driven from the anode to the cathode. At $Da_a < 100$ the flow becomes reversed and redirected from the cathode to anode [see inset of Figs. 9(b) and 15]. A similar trend was reported

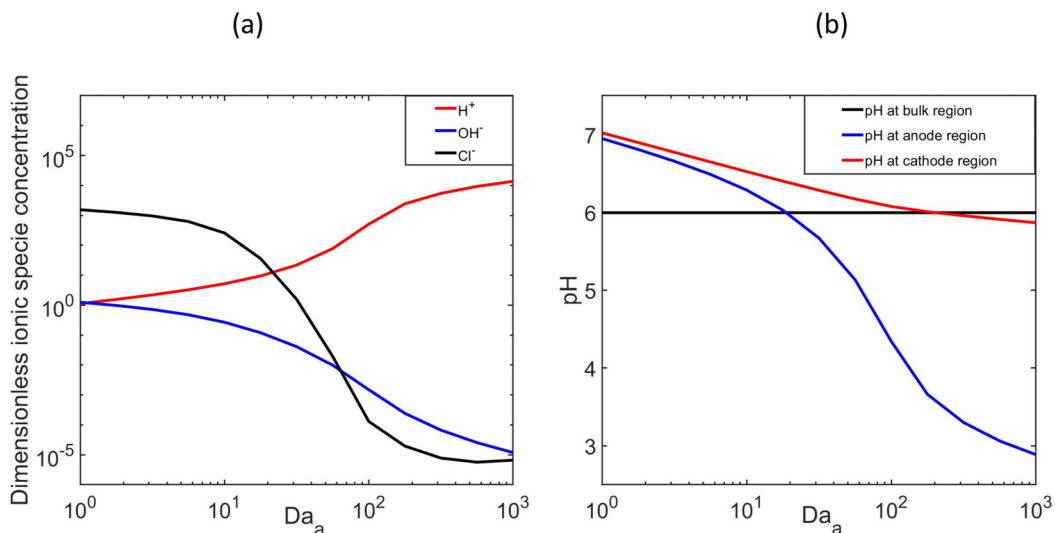


FIG. 10. Effects of Da_a on (a) ionic species concentration and (b) average pH at the electrodes and bulk region.

for a Pt-Au H_2O_2 system in pure water that is devoid of additional ionic species, which confirms the flow reversal to be reaction driven at lower anodic Damköhler numbers [18].

The possible flow reversal was explored experimentally by tuning some parameters in Eq. (8) to generate a lower Da_a reactive regime. The parameters of interest are the concentration of H_2O_2 and the pH that impacts the bulk ion concentration \tilde{c}_∞ . Other parameters such as the diffusion coefficient and the bielectrode length are made constant in this regard. The rate constant depends on the reactivity and surface properties of the metal [18]. We prepared a solution of H_2O_2 and negative tracers, whose molarity (2 mM) and bulk pH (pH = 5) corresponds to a low anodic reactivity regime ($Da_a = 58$). The bulk pH was experimentally adjusted through the addition of HCl. During the electrocatalytic reaction, the fluid flow is indeed completely reversed, where negatively charged particles are observed to be transported from Au to Pt that contrasts the normal electro-osmotic flow pattern (see Supplemental Material video 2 [29]).

The cause of the flow reversal is further traced by examining the ionic species concentration and pH profile at the electrodes and bulk region within the catalytic system (Fig. 10). At $Da_a < 100$, the amount of inert chloride ions dominates that of H^+ and OH^- , and it causes an imbalance in the charge density that contributes to the flow reversal. As the oxidation rate is increased ($Da_a > 100$) the effect of chloride ions diminishes [Fig. 10(a)]. The proton gradient that triggers the electrokinetic processes diminishes at lower Da_a regimes, thereby contributing to the observed flow reversal, while for higher Da_a numbers, the proton gradient becomes more pronounced, which corresponds to the reaction regime where the normal flow is obtained [Fig. 10(b)].

V. CONCLUSIONS

Electrocatalytic reaction-driven flow has been studied by focusing on experimental and numerical analysis that give fundamental insights on the key elements. These include the generated electric field, reaction kinetics, and diffusio-electro-osmotic phenomena that control the resulting mass transport characteristics. The electrocatalytic current between the electrodes and the induced potential that governs the reactive fluxes are measured electrochemically while the fluid flow is visualized via particle tracking. The velocity magnitude is influenced by changes in electrolyte concentration and pH. Numerical simulations reveal the synergy between the electrodes' surface reactivity contrast

which controls the production and depletion of protons with the resulting fluid flow. Flow reversal occurs at low anodic Damköhler numbers and is associated with a weak proton gradient coupled with a charge density imbalance. The key findings regarding the electrolyte concentration, bulk proton concentration, and electrode reactivity are crucial for electrocatalytic processes.

ACKNOWLEDGMENTS

This work is part of the research program Stirring the Boundary Layer with project number STW 016.160.312, which is financed by the Dutch Research Council (NWO). Jan van Nieuwkastele is acknowledged for technical assistance with the bielectrode fabrication. We thank Alvaro Marin for his helpful discussions on the GDPT technique.

APPENDIX A: IONIC SPECIES BULK CONCENTRATIONS

HCl is a strong acid that dissociates completely in water yielding H^+ , OH^- , and Cl^- (A1). The reaction proceeds with a large dissociation constant (A2):



$$K_a = \frac{[\text{H}^+][\text{Cl}^-]}{[\text{HCl}]} = 1.3 \times 10^6 \text{ mol/m}^3. \quad (\text{A2})$$

To determine the bulk concentration of the respective ionic species from HCl dissociation, we consider three limiting conditions. First, water dissociation equilibrium must be satisfied ($K_w = 1 \times 10^{-14} \text{ mol}^2/\text{m}^6$) (A3):

$$K_w = [\text{H}^+][\text{OH}^-]. \quad (\text{A3})$$

Second, mass balance must be established between the undissociated acid and its conjugate base Cl^- . For this reason their sum is constant and equivalent to the nominal concentration c_{nom} (A4). The nominal concentration c_{nom} refers to the initial acid concentration used for adjusting the pH during experiments:

$$c_{\text{nom}} = [\text{HCl}] + [\text{Cl}^-]. \quad (\text{A4})$$

We then assume the complete dissociation of HCl, by neglecting the first term in the right-hand side of Eq. (A4):

$$c_{\text{nom}} = [\text{Cl}^-]. \quad (\text{A5})$$

The electroneutrality condition must hold for the ionic solution where the sum of the corresponding ionic species charges equates to zero (A6):

$$[\text{H}^+] = [\text{OH}^-] + [\text{Cl}^-]. \quad (\text{A6})$$

Combining Eqs. (A3) (A5), and (A6) gives an expression that connects the proton concentration with the acid's concentration c_{nom} (A7):

$$[\text{H}^+] = [\text{OH}^-] + [c_{\text{nom}}]. \quad (\text{A7})$$

OH^- can be eliminated by combining Eqs. (A3) and (A7) to give Eq. (A8):

$$[\text{H}^+] = c_{\text{nom}} + \frac{K_w}{[\text{H}^+]}. \quad (\text{A8})$$

Equation (A8) implies that proton concentration will be equal to the nominal acid's bulk concentration. Assuming $c_{\text{nom}} = \tilde{c}_\infty$, whose ionic strength is highly dependent on the starting pH of the peroxide solution, Eq. (A8) can be reformulated in a quadratic form $[\text{H}^+]^2 - \tilde{c}_\infty[\text{H}^+] - K_w = 0$,

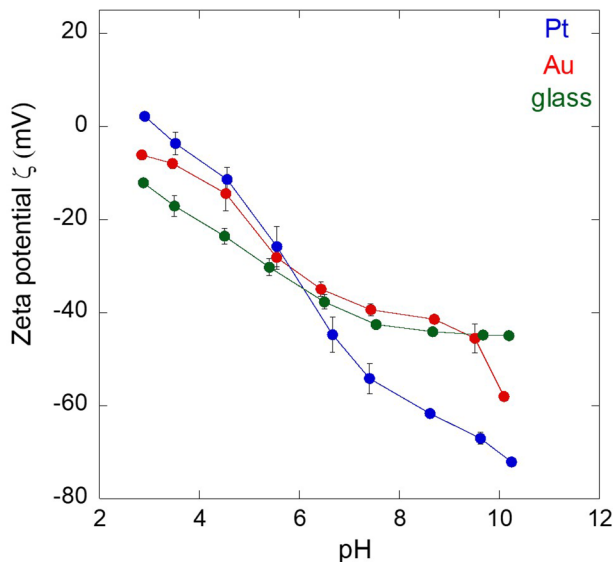


FIG. 11. ζ potential measurements as a function of pH for Pt, Au, and glass.

having roots

$$\tilde{c}_{\text{H}^+} = \frac{\tilde{c}_{\infty} + \sqrt{(\tilde{c}_{\infty})^2 + (4K_w)}}{2}. \quad (\text{A9})$$

APPENDIX B: ELECTRODE ζ POTENTIAL MEASUREMENT

Here we evaluated the ζ potential determined for Au and Pt electrodes from streaming current measurements. This was conducted within an adjustable cell using an electrokinetic analyzer equipment (SurPASS, Anton Paar). The streaming current is generated when a dilute electrolyte is driven by a pressure difference dp/L between two planar substrate containing the electrodes, while the ζ potential is computed using the Helmholtz-Smoluchowski equation:

$$\zeta = \frac{dI}{dp} \times \frac{\eta}{\varepsilon} \times \frac{L}{A}. \quad (\text{B1})$$

The cell constant is denoted as L/A , where A is the cross-sectional area and L the channel length, and dI/dp is the streaming current change with applied pressure. The ζ potential was evaluated as a function of pH in a 5 mM KCl solution by titrating the solution with NaOH or HCl (0.1 M) in order to vary the pH of the solution. The ζ potential measurements for the metals and glass are shown in Fig. 11 where the ζ potential becomes highly negative at higher pH regime and less negative at lower pH.

APPENDIX C: TRACER PARTICLE ζ POTENTIAL MEASUREMENT

The mean ζ potential for negative and positive tracer particles (carboxyl-modified polystyrene, FluoSpheres, and amidine latex beads, Fischer Scientific), are measured in 5 mM KCl at pH 6 (Fig. 12). We found that the particles' ζ potential is not severely affected by the pH range (5–6) within which our experiments were conducted.

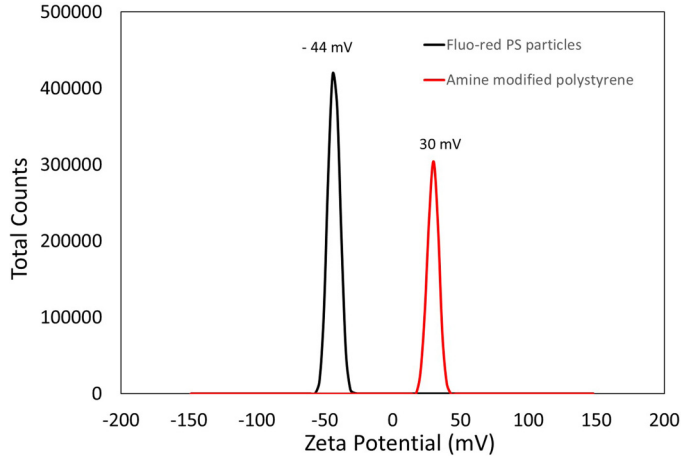


FIG. 12. Tracer particle ζ potential distribution, negative particles (carboxylated-modified polystyrene), positive tracer particles (amidine modified polystyrene).

APPENDIX D: COMPARISON OF EXPERIMENTAL AND NUMERICAL RESULTS FOR THE VELOCITY MAGNITUDE

The velocity of the tracer particles is described by Newton's second law,

$$m_p \frac{d\mathbf{u}_p}{dt} = \mathbf{F}, \quad (\text{D1})$$

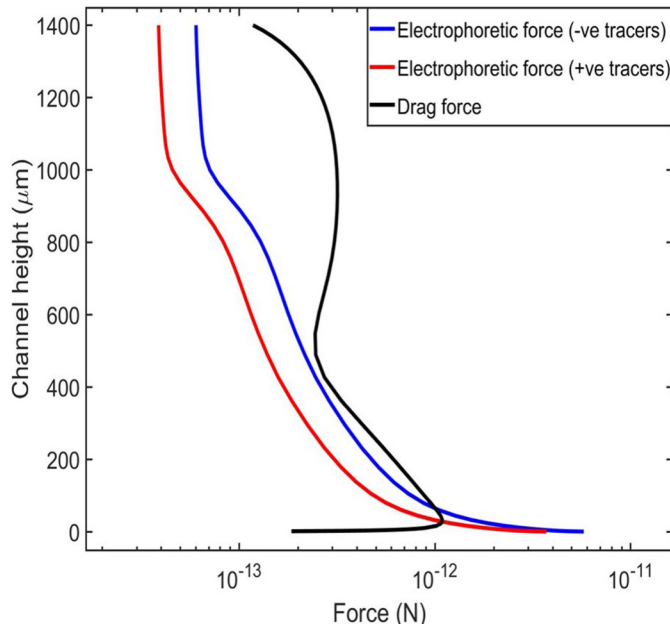


FIG. 13. Variation of the forces acting on the tracer particles along the channel height.

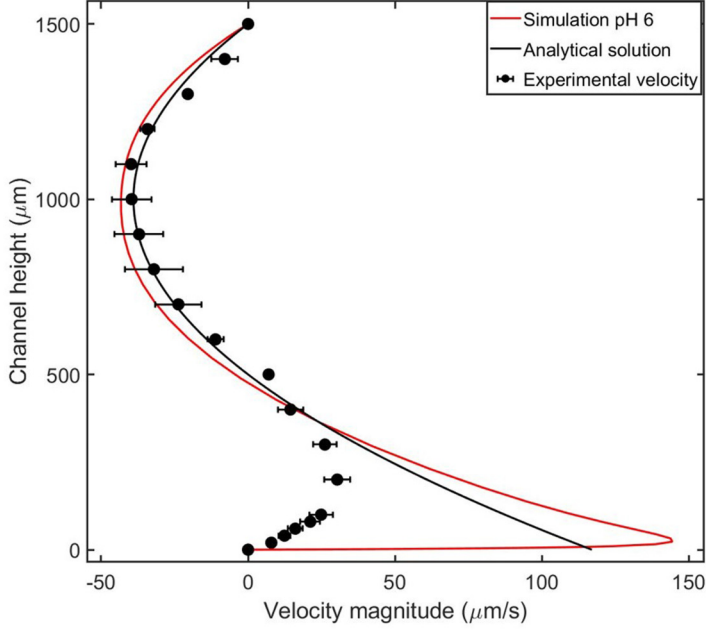


FIG. 14. Velocity magnitude for Pt-Au bielectrode in $0.3 \text{ M H}_2\text{O}_2$ (pH 6) for experiments fitted with an analytical solution and simulations. The filled symbols indicate experimental data, the red solid line depicts simulation data, and the solid black line is the analytical solution fitted to the experimental data.

where m_p is the particle mass and \mathbf{F} is the net force acting on the particle, which consists of both the drag force \mathbf{F}_d and the electrophoretic force \mathbf{F}_{ep}

$$\mathbf{F} = \mathbf{F}_d + \mathbf{F}_{\text{ep}}. \quad (\text{D2})$$

The drag force acting on the particles of radius r moving through peroxide solution with velocity \mathbf{u} is expressed as

$$\mathbf{F}_d = 6\pi r\eta\mathbf{u}. \quad (\text{D3})$$

The electrophoretic force is derived based on the product of the Stokes' drag constant $d = 6\pi$ and the electrophoretic velocity $\mathbf{u}_{\text{ep}} = \frac{\epsilon}{\eta}\zeta\rho_+\mathbf{E}$ as

$$\mathbf{F}_{\text{ep}} = 6\pi r\eta\mathbf{u}_{\text{ep}}. \quad (\text{D4})$$

The variation of the aforementioned forces along the channel height are plotted and shown in Fig. 13.

Here we formulate a simple analytical expression that can be fitted with the upper parabola of the experimental fluid flow velocity to determine the surface velocity u_s along the channel height in the y -direction. We begin with a simplified form of the Stokes equation, where the advective-inertial term is neglected for a steady-state condition and $\nabla p = 0$ to obtain a second-order partial differential equation (PDE):

$$\eta \frac{\partial^2 u}{\partial y^2} = 0. \quad (\text{D5})$$

This parabolic PDE can be reformulated in a form of a quadratic equation

$$a\tilde{y}^2 + b\tilde{y} + c = 0. \quad (\text{D6})$$

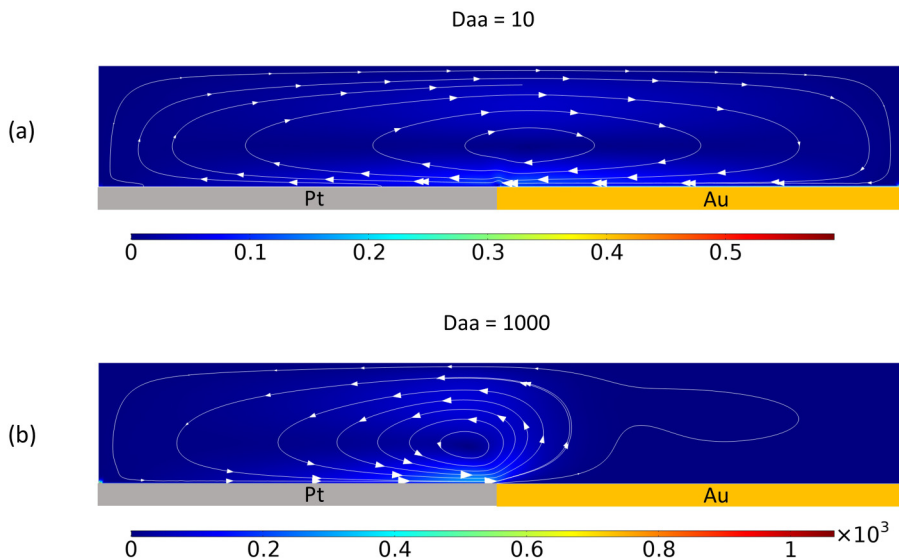


FIG. 15. Flow hysteresis generated by changes in Da_a as indicated by the velocity vector plot (a) flow reversal at $Da_a = 10$; (b) electro-osmotic flow at $Da_a = 1000$.

Equation (D6) is solved with boundary conditions $u = u_s$ at $y = 0$, and $u = 0$ at $y = 1$. By integrating Eq. (D6) along the channel height,

$$\int_0^1 (a\bar{y}^2 + b\bar{y} + c) d\bar{y} = 0, \quad (\text{D7})$$

and solving for a and b gives

$$u(y) = u_s(3y^2 - 4y + 1). \quad (\text{D8})$$

We have used this equation to fit the experimental velocity values in the upper part of the volume, in order to extract the surface velocity at the electrode (see Fig. 14).

APPENDIX E: FLUID FLOW REVERSAL

At $Da_a < 10$, the catalytically induced fluid flow is reversed and is driven from the cathode (Au) to the anode (Pt) (Fig. 15). The flow magnitude generated at the bielectrode junction is lower and its direction differs from the normal electro-osmotic flow pattern induced for $Da_a = 1000$ (Fig. 15).

-
- [1] H. Hess and G. D. Bachand, Biomolecular motors, *Mater. Today* **8**, 22 (2005).
 - [2] M. Mickler, E. Schleiff, and T. Hugel, From biological towards artificial molecular motors, *ChemPhysChem* **9**, 1503 (2008).
 - [3] W. F. Paxton, K. C. Kistler, C. C. Olmeda, A. Sen, S. K. St. Angelo, Y. Cao, T. E. Mallouk, P. E. Lammert, and V. H. Crespi, Catalytic nanomotors: Autonomous movement of striped nanorods, *J. Am. Chem. Soc.* **126**, 13424 (2004).
 - [4] W. F. Paxton, P. T. Baker, T. R. Kline, Y. Wang, T. E. Mallouk, and A. Sen, Catalytically induced electrokinetics for motors and micropumps, *J. Am. Chem. Soc.* **128**, 14881 (2006).
 - [5] W. Wang, W. Duan, Z. Zhang, M. Sun, A. Sen, and T. E. Mallouk, A tale of two forces: Simultaneous chemical and acoustic propulsion of bimetallic micromotors, *Chem. Commun.* **51**, 1020 (2015).

- [6] J. Wu, S. Balasubramanian, D. Kagan, K. M. Manesh, S. Campuzano, and J. Wang, Motion-based DNA detection using catalytic nanomotors, *Nat. Commun.* **1**, 36 (2010).
- [7] J. Guo, J. J. Gallegos, A. R. Tom, and D. Fan, Electric-field-guided precision manipulation of catalytic nanomotors for cargo delivery and powering nanoelectromechanical devices, *ACS Nano* **12**, 1179 (2018).
- [8] J. Wang, Cargo-towing synthetic nanomachines: Towards active transport in microchip devices, *Lab Chip* **12**, 1944 (2012).
- [9] J. Burdick, R. Laocharoensuk, P. M. Wheat, J. D. Posner, and J. Wang, Synthetic nanomotors in microchannel networks: Directional microchip motion and controlled manipulation of cargo, *J. Am. Chem. Soc.* **130**, 8164 (2008).
- [10] Y. Wang, R. M. Hernandez, D. J. Bartlett, J. M. Bingham, T. R. Kline, A. Sen, and T. E. Mallouk, Bipolar electrochemical mechanism for the propulsion of catalytic nanomotors in hydrogen peroxide solutions, *Langmuir* **22**, 10451 (2006).
- [11] M. E. Ibele, Y. Wang, T. R. Kline, T. E. Mallouk, and A. Sen, Hydrazine fuels for bimetallic catalytic microfluidic pumping, *J. Am. Chem. Soc.* **129**, 7762 (2007).
- [12] C. Zhou, H. Zhang, Z. Li, and W. Wang, Chemistry pumps: A review of chemically powered micropumps, *Lab Chip* **16**, 1797 (2016).
- [13] I.-K. Jun and H. Hess, A biomimetic, self-pumping membrane, *Adv. Mater.* **22**, 4823 (2010).
- [14] A. A. Farniya, M. J. Esplandiú, D. Reguera, and A. Bachtold, Imaging the Proton Concentration and Mapping the Spatial Distribution of the Electric Field of Catalytic Micropumps, *Phys. Rev. Lett.* **111**, 168301 (2013).
- [15] J. L. Moran and J. D. Posner, Electrokinetic locomotion due to reaction-induced charge autoelectrophoresis, *J. Fluid Mech.* **680**, 31 (2011).
- [16] J. L. Moran, P. M. Wheat, and J. D. Posner, Locomotion of electrocatalytic nanomotors due to reaction induced charge autoelectrophoresis, *Phys. Rev. E* **81**, 065302(R) (2010).
- [17] M. J. Esplandiú, A. Afshar Farniya, and D. Reguera, Key parameters controlling the performance of catalytic motors, *J. Chem. Phys.* **144**, 124702 (2016).
- [18] S. M. Davidson, R. G. Lammertink, and A. Mani, Predictive model for convective flows induced by surface reactivity contrast, *Phys. Rev. Fluids* **3**, 053701 (2018).
- [19] J. Wiedemair, H. D. S. van Dorp, W. Olthuis, and A. van den Berg, Developing an amperometric hydrogen peroxide sensor for an exhaled breath analysis system, *Electrophoresis* **33**, 3181 (2012).
- [20] J. H. Park, H. Zhou, S. J. Percival, B. Zhang, F.-R. F. Fan, and A. J. Bard, Open circuit (mixed) potential changes upon contact between different inert electrodes-size and kinetic effects, *Anal. Chem.* **85**, 964 (2013).
- [21] R. Barnkob, C. J. Kähler, and M. Rossi, General defocusing particle tracking, *Lab Chip* **15**, 3556 (2015).
- [22] K. Schätzel and J. Merz, Measurement of small electrophoretic mobilities by light scattering and analysis of the amplitude weighted phase structure function, *J. Chem. Phys.* **81**, 2482 (1984).
- [23] J. C. Corbett, F. McNeil-Watson, R. O. Jack, and M. Howarth, Measuring surface zeta potential using phase analysis light scattering in a simple dip cell arrangement, *Colloids Surf. A* **396**, 169 (2012).
- [24] W. F. Paxton, A. Sen, and T. E. Mallouk, Motility of catalytic nanoparticles through self-generated forces, *Chem. Eur. J.* **11**, 6462 (2005).
- [25] C. L. Druzgalski, M. B. Andersen, and A. Mani, Direct numerical simulation of electroconvective instability and hydrodynamic chaos near an ion-selective surface, *Phys. Fluids* **25**, 110804 (2013).
- [26] J. H. Masliyah and S. Bhattacharjee, *Electrokinetic and Colloid Transport Phenomena* (John Wiley and Sons, New York, 2005).
- [27] J. Duval, J. M. Kleijn, and H. P. Van Leeuwen, Bipolar electrode behaviour of the aluminium surface in a lateral electric field, *J. Electroanal. Chem.* **505**, 1 (2001).
- [28] A. Bard and L. Faulkner, *Electrochemical Methods: Fundamentals and Applications* (Wiley, 2000).
- [29] See Supplemental Material at <http://link.aps.org/supplemental/10.1103/PhysRevFluids.6.044004> for movies 1 and 2.
- [30] I. Sbalzarini and P. Koumoutsakos, Feature point tracking and trajectory analysis for video imaging in cell biology, *J. Struct. Biol.* **151**, 182 (2005).

- [31] K. Tatsumi, K. Nishitani, K. Fukuda, Y. Katsumoto, and K. Nakabe, Measurement of electroosmotic flow velocity and electric field in microchannels by micro-particle image velocimetry, *Meas. Sci. Technol.* **21**, 105402 (2010).
- [32] P. Biesheuvel, M. van Soestbergen, and M. Bazant, Imposed currents in galvanic cells, *Electrochim. Acta* **54**, 4857 (2009).
- [33] P. Delahay, *Double Layer and Electrode Kinetics* (Interscience Publ., 1966), p. 321.
- [34] M. Z. Bazant, K. T. Chu, and B. J. Bayly, Current-voltage relations for electrochemical thin films, *SIAM J. Appl. Math.* **65**, 1463 (2005).